PROCEEDINGS OF SPIE

SPIEDigitalLibrary.org/conference-proceedings-of-spie

X-ray dark-field tomography using edge-illumination

Adam Doherty, Savvis Savidis, Alberto Astolfo, Lorenzo Massimi, Nargiza Djurabekova, et al.

Adam Doherty, Savvis Savidis, Alberto Astolfo, Lorenzo Massimi, Nargiza Djurabekova, Carlos Navarrete Leon, Mattia F. M. Gerli, Francesco Iacoviello, Paul Shearing, Danielle Norman, Mark A. Williams, Alessandro Olivo, Marco Endrizzi, "X-ray dark-field tomography using edge-illumination," Proc. SPIE 12242, Developments in X-Ray Tomography XIV, 1224209 (10 November 2022); doi: 10.1117/12.2632731

SPIE.

Event: SPIE Optical Engineering + Applications, 2022, San Diego, California, United States

X-ray Dark-Field Tomography Using Edge-Illumination

Adam Doherty[a], Savvas Savvidis[a], Alberto Astolfo[a], Lorenzo Massimi[a], Nargiza Djurabekova[b], Carlos Navarrete-León[a], Mattia F. M. Gerli[c,d], Francesco Iacoviello[e], Paul R. Shearing[e], Danielle G. Norman[f], Mark A. Williams[f], Alessandro Olivo[a], and Marco Endrizzi[a]

[a]Department of Medical Physics and Biomedical Engineering, University College London, London, WC1E 6BT, UK
[b]Department of Computer Science, University College London, London, WC1E 6BT, UK
[c]UCL Division of Surgery and Interventional Science, Royal Free Hospital, London, UK
[d]Stem Cell and Regenerative Medicine Section, Great Ormond Street Institute of Child Health, University College London, London, WC1N 1EH, UK
[e]The Electrochemical Innovation Lab, Department of Chemical Engineering, University College London, London, UK
[f]WMG, University of Warwick, Coventry, UK

ABSTRACT

X-ray dark-field imaging is used to visualise the ultra-small angle x-ray scattering signal that originates from sub-resolution density fluctuations within the sample microstructure. Dark-field tomography using the edge-illumination x-ray imaging system is presented as a tool for measuring this scattering signal in a sample in three dimensions. Its applicability to different fields is shown through example images of a multi-material phantom, a tissue-engineered oesophagus, a pouch cell battery and a short-fibre reinforced composite material. The multi-channel contrast available in edge-illumination helps with material identification, with high contrast at boundaries enhancing dark-field reconstructions.

Keywords: x-ray tomography, x-ray dark-field imaging, x-ray phase-contrast imaging

1. INTRODUCTION

Dark-field imaging is a novel imaging modality where contrast arises from ultra-small angle x-ray scattering within the sample,[1–3] which occurs when there are density fluctuations within the microstructure of the sample, such as fibres, pores, bubbles, cracks, powder or sharp edges.[4–9] Such scatterers have dimensions smaller than the system resolution as dark-field imaging probes information from unresolvable sample features. Consequently, a dark-field imaging system with a typical pixel size of approximately 100µm can represent a centimetre-sized object based on its micro and nanostructure.

The scattering associated with the dark-field signal is in the forward direction, therefore specialised setups such as the edge-illumination x-ray imaging system are required with sensitivity to small scattering angles[10,11] (See Figure 1(a)). Edge-illumination makes use of a conventional incoherent source and flat panel detector, with two absorbing periodic masks placed on either side of the sample. These masks, labelled the sample and detector masks, have vertical apertures that modulate the beam into a series of beamlets whose shape and position are then precisely measured. Comparing their shape and position with and without the sample, the dark-field signal is extracted by quantifying the broadening imposed on the angular distribution of the x-rays by the sample. Refraction can also be measured by quantifying the overall lateral shift of the x-ray beamlets. Both these quantities can be measured in one direction only, perpendicular to both the beam propagation and the apertures in the mask. Conventional attenuation images are also retrieved as the ratio of intensity in the beamlets with and without the sample. As such, edge-illumination can be used for multi-channel contrast with the three images of attenuation, phase-contrast and dark-field signals supplying complementary information.

Further information contact adam.doherty@ucl.ac.uk

Developments in X-Ray Tomography XIV, edited by Bert Müller, Ge Wang, Proc. of SPIE Vol. 12242, 1224209
 · 0277-786X · doi: 10.1117/12.2632731

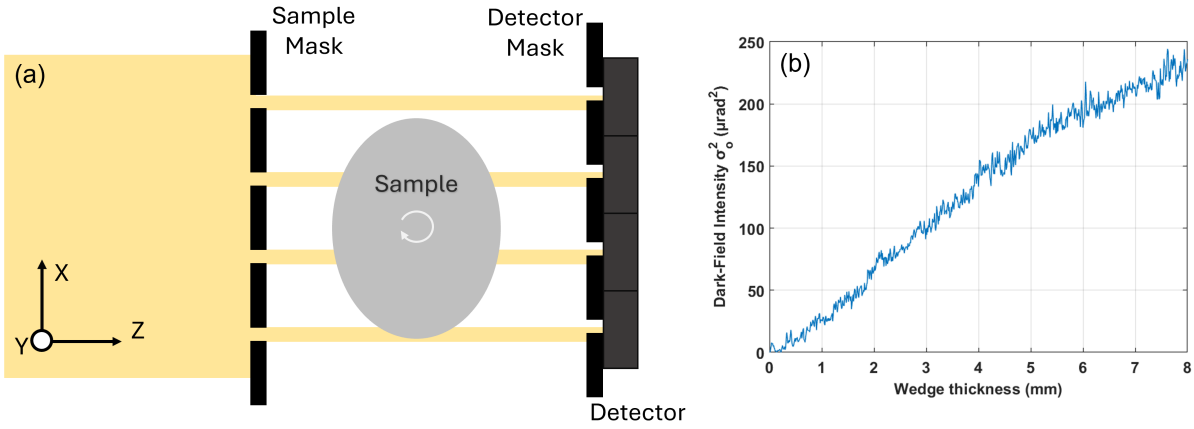

Figure 1. (a) Top-down view of edge-illumination setup, with x-rays travelling through the sample mask apertures, where the beam is split into a series of beamlets before incident on the sample. These beamlets partially illuminate the detector, with the fraction of intensity reaching the detector pixels modulated by moving the sample mask along the x-axis, with the rest of the beamlet absorbed by the detector mask. In tomographic acquisition, the sample is rotated around the y-axis as shown. In (b), a dark-field intensity profile from a wedge sample shows linearity up to roughly 4 mm of wedge thickness. Beyond this point, at high dark-field signals, the imaging system response begins to be affected by signal saturation.

2. THEORY

An edge-illumination imaging system is characterised by its illumination curve, which is experimentally obtained by recording the x-ray intensity that reaches each detector pixel as a function of the relative displacement of the two masks. For a scattering sample, the illumination curve, $I_s(x)$, can be modelled as the convolution between the source, mask apertures and sample as follows:

$$I_s(x) = M_1(x) * O(x) * M_2(x) * S(x). \tag{1}$$

Where $*$ denotes convolution operation, with M_1 and M_2 denoting the sample and detector mask apertures respectively, $O(x)$ representing the object scattering function and $S(x)$ the projected source at the detector. The resulting illumination curve is fitted with a Gaussian model, with its variance used to quantify the width of the beam for dark-field signal retrieval. The illumination curve without the sample is also measured with its width used as a reference to quantify the broadening caused by the presence of the sample.

In edge-illumination, the dark-field image is a pixel-by-pixel representation of the sample that equates to the variance of the object scattering functions, σ_o^2. Under a Gaussian approximation for both the scattering function $O(x)$ and the system's illumination curve, the dark-field image is calculated as the difference in the variance of the illumination curve with and without the sample.

This measurement of σ_o^2 is the projection of the dark-field signal along the x-ray propagation axis, tomographic reconstruction is required to recover depth information and build a 3D volume. Conventional tomographic reconstruction algorithms such as filtered-back projection rely on the assumption that the measured signal in the projections, here the dark-field signal, is linear with optical path length. The summation nature of the variance in Gaussian convolution satisfies this requirement.

If the sample is split into a series of N layers, each labelled, i, the projected scattering function is a convolution of a series of N scattering functions, each associated with one layer. As such, the measured dark-field signal is a sum of the variances measured at each layer. In the limit these layers are made infinitely small this summation turns into an integral over the path length. This equation is analogous to that of the linear attenuation coefficient seen in conventional CT reconstruction:

$$\sigma_o^2(x, y; \theta) = \int \epsilon(x, y, z)\, dl. \tag{2}$$

Where the linear scattering coefficient ϵ has been introduced. This is the parameter reconstructed in dark-field tomography and indicates the strength of the scattering at each point within the sample.

3. METHODS

The edge-illumination system was set up as described by Havariyoun et. al.[12] A Rigaku Molybdenum rotating anode source operating at 40keV and 25mA was used alongside a Hamamatsu CMOS-based flat panel detector. In order to expose the whole sample, it was translated in sub-pixel steps along the x-axis and these steps then stitched together to form an image, a process known as dithering.[13] This also increases the resolution of the system, which is determined by the sample mask aperture size of 10µm. After dithering and accounting for magnification, reconstructed volumes had voxel dimensions of 10µm in the slice plane and 40µm in the axial direction.

The model described in Section 2 was validated through the use of a homogeneous wedge phantom. Following Equation 2, a linear increase in thickness should bring a linear increase in dark-field signal. A planar image of a wedge filled with cornflower rising to roughly 1cm thick was acquired using 8 dithering steps and 9 illumination curve points, each with 2 seconds of exposure.

A series of samples were then scanned for tomography: a multi-material phantom, consisting of HDPE, PP and cornflower cylinders; a short-fibre reinforced composite; a pouch cell battery and a tissue-engineered oesophagus (See Savvidis et al. for oesophageal sample preparation[14]). The regular acquisition parameters were set as 8 dithering steps, 7 illumination curve points, 720 angular projections and 1.2 seconds of exposure, however, the high attenuation of the pouch cell battery meant that 9 illumination curve points were used to increase the statistics of the acquisition, and for the oesophagus where 1000 angular views were used for preserving the spatial resolution.

4. RESULTS

The dark-field signal from the wedge phantom is linear with sample thickness, shown in Figure 1(b). This validates Equation 2 and as a result, the use of conventional filtered-back projection is possible for reconstructing dark-field volumes. The observed saturation is a combined effect of beam hardening, which progressively reduces the dark-field signal by removing the lower energy components of the spectrum, and of the limited dynamic range of the imaging system. This saturation point is high enough to be beyond the dark-field signal from typical samples.

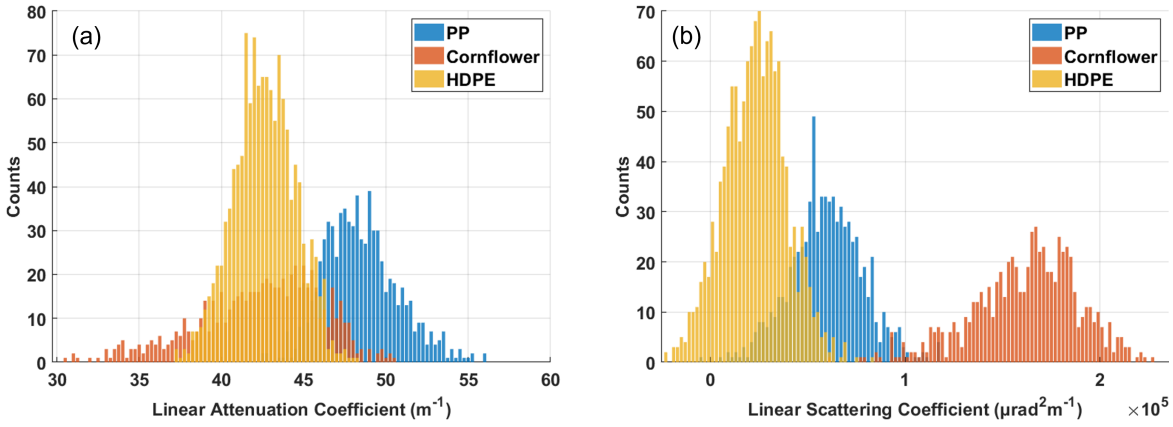

Figure 2. Histograms for intensity in (a) attenuation and (b) dark-field tomographic reconstructions for the multi-material phantom. The cornflower sample intensity in attenuation overlaps with the other materials, particularly the HDPE, however, it is well distinguished from the other samples through the dark-field signal. This is an example of how the sensitivity of dark-field imaging to microstructure can help in separating materials that would otherwise be completely overlapped if observed purely based on their linear attenuation coefficient.

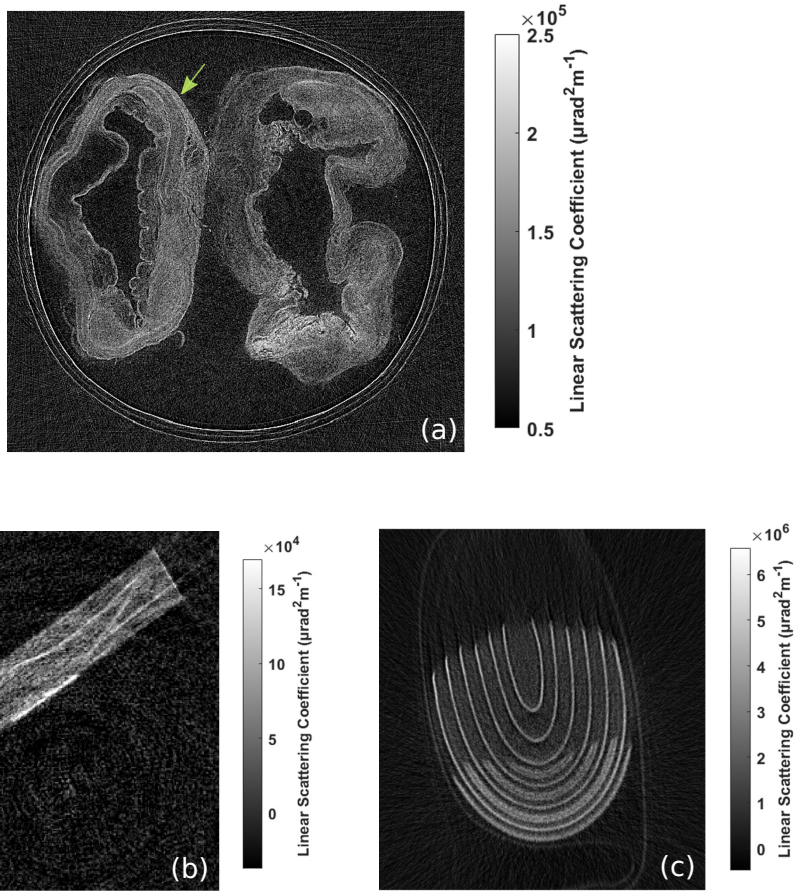

Figure 3. Some examples of dark-field tomographic reconstructions. A tissue-engineered oesophagus in (a), where one can see the separation of submucosa and inner and outer circular muscle layers, highlighted best around the arrow. In (b), a short-fibre reinforced composite is shown with a reinforcement framework appearing as a bright structure throughout the sample. In (c), a pouch cell battery with a strong contrast between the anode or cathode and separator material is enhanced by the strong boundary signal in dark-field imaging.

The multi-material phantom shows the different dark-field intensities arising from materials with differing microstructures, as well as the complementary nature of the dark-field and attenuation signals. After reconstructing the attenuation and dark-field signals and binning to $0.1mm^3$ voxels to match the system's resolution in all three dimensions, the intensity in the three materials is shown in the histograms in Figure 2. These show that the materials are better distinguished through dark-field tomography than conventional attenuation tomography. High dark-field intensity is visible with cornflower due to the powderous microstructure, whereas it is similar in grey level to the HDPE sample in the attenuation contrast channel. The reconstructions of the other samples are presented together in Figure 3. For the short-fibre reinforced composite, a distinct structure is seen weaving throughout the volume, which highlights the reinforcement structure of the composite. The samples also show a sharp peak in dark-field signal at sharp boundaries, which is a known phenomenon and arises due to the unresolved phase gradient. This is seen strongest with the pouch cell battery sample, where the large discrepancy in density between the metal anode and separator leads to a dark-field peak at the edges of the material. A similar result is seen in the tissue-engineered oesophagus, where the submucosa can be delineated alongside the separation between the inner and outer circular muscle layers on the outside of the sample.

5. CONCLUSIONS

Dark-field tomography is presented as a technique for visualising the ultra-small angle x-ray scattering signal within a sample. We show that the dark-field signal is linear with sample thickness, and hence it can be recon-

structed through standard tomographic reconstruction algorithms, analogous to the reconstruction of attenuation signal in conventional computed tomography. The dark-field signal is shown to be complementary to the attenuation signal allowing the separation of materials with very similar linear attenuation coefficients, thanks to the sensitivity to the material's microstructure. Three dark-field reconstructions are then presented of different samples, encompassing applications in the biomedical as well as in the mechanical and chemical engineering fields.

ACKNOWLEDGMENTS

AO is supported by the Royal Academy of Engineering under their Chairs in Emerging Technologies scheme (CiET1819/2/78). This work was supported by the National Research Facility for Lab X-ray CT (NXCT) through EPSRC grants EP/T02593X/1 and EP/V035932/1. This work was supported by the Wellcome Trust 221367/Z/20/Z. This work was supported by EPSRC grants EP/T005408/1 and EP/R513143/1.

REFERENCES

[1] Rigon, L., Besch, H.-J., Arfelli, F., Menk, R.-H., Heitner, G., and Plothow-Besch, H., "A new dei algorithm capable of investigating sub-pixel structures," *Journal of Physics D: Applied Physics* **36**(10A), A107 (2003).

[2] Pfeiffer, F., Bech, M., Bunk, O., Kraft, P., Eikenberry, E. F., Brönnimann, C., Grünzweig, C., and David, C., "Hard-x-ray dark-field imaging using a grating interferometer," *Nature materials* **7**(2), 134–137 (2008).

[3] Endrizzi, M., Diemoz, P. C., Millard, T. P., Louise Jones, J., Speller, R. D., Robinson, I. K., and Olivo, A., "Hard x-ray dark-field imaging with incoherent sample illumination," *Applied Physics Letters* **104**(2), 024106 (2014).

[4] Matsunaga, N., Yano, K., Endrizzi, M., and Olivo, A., "Detection of individual sub-pixel features in edge-illumination x-ray phase contrast imaging by means of the dark-field channel," *Journal of Physics D: Applied Physics* **53**(9), 095401 (2019).

[5] Massimi, L., Clark, S. J., Marussi, S., Doherty, A., Schulz, J., Marathe, S., Rau, C., Endrizzi, M., Lee, P. D., and Olivo, A., "Dynamic multicontrast x-ray imaging method applied to additive manufacturing," *Physical Review Letters* **127**(21), 215503 (2021).

[6] Millard, T., Endrizzi, M., Everdell, N., Rigon, L., Arfelli, F., Menk, R. H., Stride, E., and Olivo, A., "Evaluation of microbubble contrast agents for dynamic imaging with x-ray phase contrast," *Scientific reports* **5**(1), 1–8 (2015).

[7] Shoukroun, D., Massimi, L., Endrizzi, M., Bate, D., Fromme, P., and Olivo, A., "Edge illumination x-ray phase contrast imaging for impact damage detection in cfrp," *Materials Today Communications* **31**, 103279 (2022).

[8] Senck, S., Scheerer, M., Revol, V., Plank, B., Hannesschläger, C., Gusenbauer, C., and Kastner, J., "Microcrack characterization in loaded cfrp laminates using quantitative two-and three-dimensional x-ray dark-field imaging," *Composites Part A: Applied Science and Manufacturing* **115**, 206–214 (2018).

[9] Revol, V., Plank, B., Kaufmann, R., Kastner, J., Kottler, C., and Neels, A., "Laminate fibre structure characterisation of carbon fibre-reinforced polymers by x-ray scatter dark field imaging with a grating interferometer," *Ndt & E International* **58**, 64–71 (2013).

[10] Olivo, A. and Speller, R., "A coded-aperture technique allowing x-ray phase contrast imaging with conventional sources," *Applied Physics Letters* **91**(7), 074106 (2007).

[11] Olivo, A., "Edge-illumination x-ray phase-contrast imaging," *Journal of Physics: Condensed Matter* **33**(36), 363002 (2021).

[12] Havariyoun, G., Vittoria, F. A., Hagen, C. K., Basta, D., Kallon, G. K., Endrizzi, M., Massimi, L., Munro, P., Hawker, S., Smit, B., et al., "A compact system for intraoperative specimen imaging based on edge illumination x-ray phase contrast," *Physics in Medicine & Biology* **64**(23), 235005 (2019).

[13] Hagen, C. K., Vittoria, F. A., i Morgó, O. R., Endrizzi, M., and Olivo, A., "Cycloidal computed tomography," *Physical Review Applied* **14**(1), 014069 (2020).

[14] Savvidis, S., Gerli, M. F., Pellegrini, M., Massimi, L., Hagen, C. K., Endrizzi, M., Atzeni, A., Ogunbiyi, O. K., Turmaine, M., Smith, E. S., et al., "Monitoring tissue engineered constructs and protocols with laboratory-based x-ray phase contrast tomography," *Acta Biomaterialia* **141**, 290–299 (2022).